Engineering 38 (2024) 184–193

Contents lists available at ScienceDirect

Engineering

journal homepage: www.elsevier.com/locate/eng

Research
Environmental Engineering—Article

Efficient Metal Recovery from Industrial Wastewater: Potential Oscillation and Turbulence Mode for Electrochemical System

Li Chen *, Gong Zhang, Huijuan Liu *, Shiyu Miao, Qingbai Chen, Huachun Lan, Jiuhui Qu

Center for Water and Ecology, State Key Joint Laboratory of Environment Simulation and Pollution Control, School of Environment, Tsinghua University, Beijing 100084, China

ARTICLE INFO

Article history:
Received 27 May 2023
Revised 12 October 2023
Accepted 7 December 2023
Available online 3 January 2024

Keywords:
Ion transport
Reaction kinetics
Transient electric field
Swirling flow

ABSTRACT

Efficient metal recovery from industrial wastewater facilitates addressing of the environmental hazards and resource requirements of heavy metals. The conventional electrodeposition recovery method is hampered by the limitations of interfacial ion transport in charge-transfer reactions, creating challenges for simultaneous rapid and high-quality metal recovery. Therefore, we proposed integrating a transient electric field (TE) and swirling flow (SF) to synchronously enhance bulk mass transfer and promote interfacial ion transport. We investigated the effects of the operation mode, transient frequency, and flow rate on metal recovery, enabling determination of the optimal operating conditions for rapid and efficient sequential recovery of Cu in TE&SF mode. These conditions included low and high electric levels of 0 and 4 V, a 50% duty cycle, 1 kHz frequency, and 400 $L \cdot h^{-1}$ flow rate. The kinetic coefficients of TE&SF electrodeposition were 3.5–4.3 and 1.37–1.97 times that of single TE and SF electrodeposition, respectively. Simulating the deposition process under TE and SF conditions confirmed the efficient concurrence of interfacial ion transport and charge transfer under TE and SF synergy, which achieved rapid and high-quality metal recovery. Therefore, the combined deposition strategy is considered an effective technique for reducing metal pollution and promoting resource recycling.

© 2024 THE AUTHORS. Published by Elsevier LTD on behalf of Chinese Academy of Engineering and Higher Education Press Limited Company. This is an open access article under the CC BY-NC-ND license (http://creativecommons.org/licenses/by-nc-nd/4.0/).

1. Introduction

Burgeoning advanced manufacturing clusters have led to a continuous increase in the consumption demand of non-ferrous metals. In China, the consumption of six common nonferrous metals (Cu, Al, Pb, Zn, Sn, and Ni) reached 11 791, 31 908, 4795, 6965, 982, and 183 thousand tonnes, respectively, in 2017, resulting in substantial production and import dependence [1,2]. The substantial amounts of water required in the production processes of these metals, including mining, ore dressing, smelting, and deep processing, result in extremely high proportions of wastewater discharge and an ever-increasing total amount of heavy metals accommodated in aquatic environments [3,4]. Discharged heavy metals in aquatic environments are non-biodegradable, easily enriched by organisms, and accumulate along the food chain, causing substantial damage to the environment and biological health [5–8]. To meet the moderate exploitation of metal mineral resources and to control and prevent their back-end pollution, efficient metal reclaiming from industrial wastewater realizes the recovery of strategic metal resources; moreover, it is essential for reusing industrial water and protecting the environment [9].

Among all the technologies employed for metal recovery, electrodeposition does not require additional chemicals or sacrificial electrodes and, as its products can be separated directly, the entire process is simplified, which is favorable for various applications [10–14]. Typical electrodeposition processes include electrochemical reactions, liquid mass transfer and dehydration, and metal nucleation and growth—among which, charge and ion transfer are the two most important steps [15]. The classical Butler–Volmer and Nernst–Planck equations describe the close relationship between reaction kinetics and electron and ion transfer in an electrochemical system [16,17]. Limited by concentration polarization, the dependence of the reaction kinetics on the voltage/current density gradually decreases (Fig. 1). In the stage controlled by the electrochemical reaction, an increase in the voltage/current density promotes electron conduction and electrochemical conversion, thereby accelerating the deposition rate. In the diffusion-controlled stage, the deposition kinetics become insensitive to an

* Corresponding authors.
E-mail addresses: l-chen19@mails.tsinghua.edu.cn (L. Chen), hjliu@tsinghua.edu.cn (H. Liu).

https://doi.org/10.1016/j.eng.2023.12.002
2095-8099/© 2024 THE AUTHORS. Published by Elsevier LTD on behalf of Chinese Academy of Engineering and Higher Education Press Limited Company.
This is an open access article under the CC BY-NC-ND license (http://creativecommons.org/licenses/by-nc-nd/4.0/).

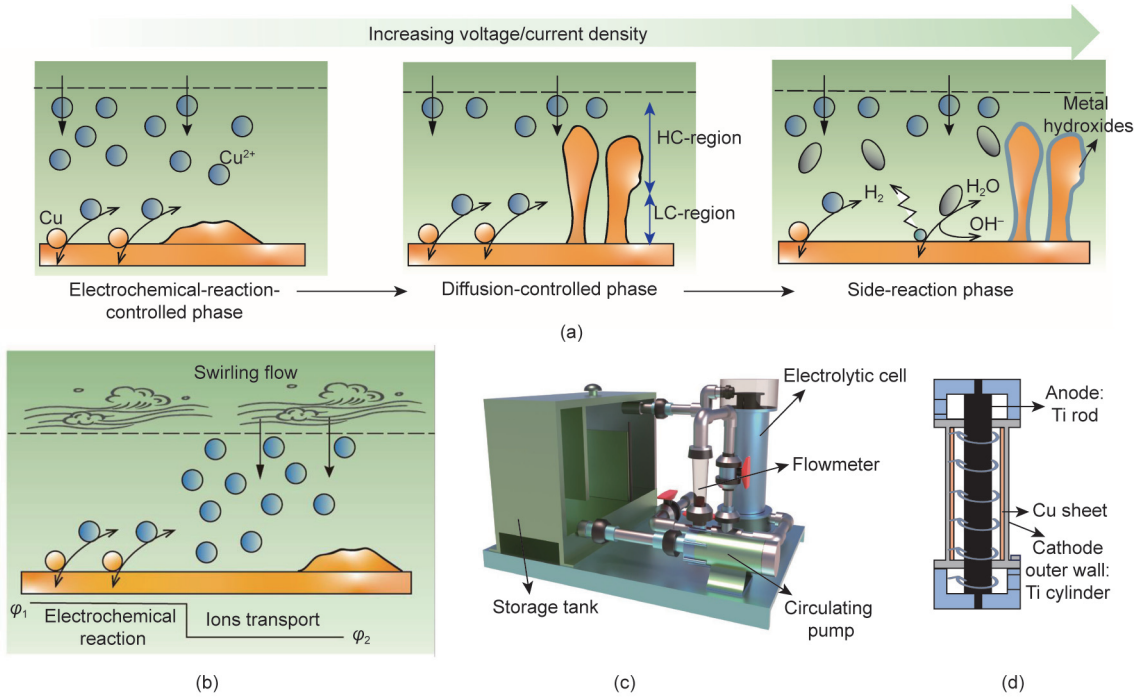

Fig. 1. (a) Schematic diagram of microscopic deposition process with an increase in voltage/current density. The reaction undergoes electrochemical-reaction-controlled, diffusion-controlled, and side-reaction phases with an increasing voltage/current density. LC- and HC-marked in the image represent low-concentration and high-concentration regions. (b) Microscopic diagram of the deposition process under the transient electric field and swirling flow. φ_1 and φ_2 marked in the image represent the high and low electric level during a periodic time of transient electric field. (c) External diagram of the deposition reactor. (d) Internal section of the electrolytic cell.

increase in voltage/current density owing to limited ion transport at the electrode, and dendritic morphology evolves in the metal deposit. Upon further increasing the voltage/current density, the cathode surface enhances hydrogen evolution and local alkalinity, leading to the formation of hydroxides and reducing product quality (Fig. 1(a)) [18]. Therefore, ion transport limits the charge transfer such that improving the electrodeposition kinetics is difficult when only the charge transfer is increased in engineering applications.

Various measures have been investigated and reported for solving the limitation of ion transport on charge transfer, including optimizing the construction of a reactor and its components and regulating the hydraulic parameters [19–21]. For example, a reactor could operate in turbulent mode to recover low-concentration metals [22]. The electrode could be rebuilt as a tubular baffle to mix the electrolyte completely within seconds during turbine operation [23]. Such measures have improved electrodeposition kinetics by enhancing convection; however, their effect on mass transfer is essentially confined to the bulk solution [24]. In other words, convection has limited ability to improve interfacial mass transfer because its working space cannot reach the reaction interface. Therefore, strengthening interfacial ion transport is critical for improving concentration polarization and enhancing reaction kinetics. To address this problem, a unique path of liquid flow has been proposed in which the solution is sprayed vertically into the cathode through an anode nozzle, thereby decreasing the thickness of the electric double layer. Consequently, the metals are recovered rapidly with excellent quality at a high current density [25].

Another technique to improve interfacial ion transport is regulating the electric field at the electrode under enhanced bulk convection (Fig. 1(b)) [26]. In the current study, a deposition strategy is proposed for enhancing the reaction kinetics by coordinating a transient electric field with a swirling flow. The deposition kinetics and properties were compared under a single transient electric field (without swirling flow, denoted as **TE**), single swirling flow (without a transient electric field, denoted as **SF**), and their synergy (denoted as **TE&SF**). Subsequently, the flow field and concentration distribution in the reactor and at the electrode interface were simulated to understand the effect of interfacial ion transport on reaction kinetics. Finally, the general applicability of the TE&SF deposition strategy was discussed and applied to metal recovery from actual industrial wastewater. In brief, the limitation of interfacial ion transport on charge transfer was solved by the synergy of the transient electric field and swirling mass transfer. This technique is an effective approach to improve the deposition kinetics and process performance.

2. Materials and methods

2.1. Chemicals and materials

The electrolytes used in this study comprised $Cu(NO_3)_2{\cdot}3H_2O$ (96%; Meryer (Shanghai) Biochemical Technology Co., Ltd., China), $Ni(NO_3)_2{\cdot}6H_2O$ (97%; Tongguang Fine Chemicals Company, China), and $C_{10}H_{14}N_2Na_2O_8{\cdot}2H_2O$ (EDTA-2Na; 99%; J&K Scientific, China). The concentrations of Cu and Ni ions were 5 $g{\cdot}L^{-1}$, whereas that of EDTA-2Na was 1.5 $g{\cdot}L^{-1}$. Deionized water produced using a laboratory pure water system (Basic-Q15-IT; Hitech Instruments Co., Ltd., China) was used as the electrolyte. The electrolyte pH was adjusted using nitric acid (76%–78%; Sinopharm Chemical Reagent Co., Ltd., China). In addition, 30 $g{\cdot}L^{-1}$ boric acid (99.5%; Meryer (Shanghai) Biochemical Technology Co., Ltd.) and 3 $g{\cdot}L^{-1}$ saccharin (98%; Meryer) were added to inhibit hydrogen evolution during Ni deposition. $AgNO_3$ powder ($\geq$ 99.8%; Xilong Scientific Co., Ltd., China) was used to prepare the Ag-containing electrolyte, with an initial concentration of 200 $mg{\cdot}L^{-1}$. Copper nitrate waste liquid was obtained from a three-waste purification company in Kunshan City (China). The concentration of heavy metals and chemical oxygen demand (COD) were approximately 30 and 1 $g{\cdot}L^{-1}$, respectively, and the pH range was 1.25−1.50.

The reactor used in this study comprised a cylindrical electrolytic cell, water storage tank, and circulating pump (Fig. 1(c)). The electrolyte (2 L) was added to the storage tank powered by a circulating pump. The electrolyte flowed in the electrolytic cell in turbulent mode at different flow rates controlled by a valve. The electrolyte cell was the main space for the electrodeposition reaction, in which a titanium rod plated with precious metals and a titanium outer wall served as the anode and cathode, respectively (Fig. 1(d)). An Hg/Hg_2SO_4 electrode was fixed in the storage tank and connected to a voltmeter with a cathode to record the cathodic potential during electrodeposition. Before operation of the reactor, a copper sheet was installed in the electrolytic cell to ensure adequate attachment to the inner wall of the cathode on which the metal ions were deposited. The total effective area of the copper sheet was 400 cm^2, and its size was 0.1 mm × 16 cm × 25 cm. Prior to electrodeposition, the copper sheet was cleaned with acetone, nitric acid, and pure water to clear the oxide layer on its surface.

2.2. Metal electrodeposition under transient electric field coupled with swirling mass transfer

An electrochemical workstation (Gamry 600+; Gamry Instruments, USA) was used to determine the cyclic voltammetry (CV) characteristics under different electrolyte conditions. Stainless steel, a platinum sheet, and Ag/AgCl electrode were used as working, counter, and reference electrodes, respectively. The CV curves were measured from –1.2 to 0.2 V vs Ag/AgCl, with a scan speed of 50 $mV{\cdot}s^{-1}$. The electrolytes used were $Cu(NO_3)_2$, $Ni(NO_3)_2$, $Cu(NO_3)_2$, and $Ni(NO_3)_2$, with the same metal ion and ethylenediaminetetraacetic acid (EDTA)-2Na concentrations of 5 and 1.5 $g{\cdot}L^{-1}$. The pH of the electrolyte solution was maintained at 2.0.

Cu and Ni from a multicomponent solution was recovered in the reactor equipped with a power supply (SOYI-VA-DM; Soyi Power, China) that generated a constant transient electric field to induce metal electrodeposition. In particular, we investigated the kinetic performance of copper recovery under different operating conditions. Under the TE condition, the electric signal operated as a square waveform with low and high voltages of 0 and 4 V, respectively, and a duty cycle of 50%. The reactor was operated in static flow mode, and the valve was only opened to mix the electrolyte during sampling. Under SF conditions, the electrodeposition process occurred at constant voltages of 2, 2.83, and 4 V, corresponding to the average, effective, and maximum values, respectively, of the square wave in periodic time. The definition and calculation equations for the average and effective values of the square wave are presented in Text S1 in Appendix A. Electrodeposition was performed under a transient electric field and swirling flow under TE&SF conditions. The effects of different frequencies (10, 100, 1000, and 10 000 Hz), flow rates (200, 400, 600, and 800 $L{\cdot}h^{-1}$), solution pH values (1.00, 1.50, and 2.35), and EDTA contents (5, 25, 50, 100 $mmol{\cdot}L^{-1}$) on the metal deposition kinetics were investigated under TE&SF electrodeposition. Samples were collected at regular intervals to determine the heavy metal concentrations. After deposition for 6 h, the copper sheet was blown with nitrogen and dried in a vacuum oven to facilitate characterization of the deposit properties. Heavy metal concentrations were measured using an inductively coupled plasma emission spectrometer (ICP-OES; 5110VDV; Agilent Technologies, USA) to calculate the recovery efficiency and kinetic coefficient (detailed formulae are presented in Text S2 in Appendix A). A power meter was used to evaluate the specific energy consumption for metal recovery under different operating modes (Text S3 in Appendix A). For the Ni-containing residual solution, we regulated the constant current density (25, 50, 75 $mA{\cdot}cm^{-2}$) to generate a stable electric field and induce continuous Ni reduction without it being affected by hydrogen evolution. The circulation flow rate of the solution was 400 $L{\cdot}h^{-1}$ and the reaction time was 6 h.

To compare the recovery performance of the TE&SF method with that of TE and SF electrodeposition, $AgNO_3$ was treated for 30 min, and samples were collected to measure the Ag concentration and obtain kinetic information. A square wave signal was applied over TE and TE&SF electrodeposition at 1 kHz with low and high voltages of 0 and 3 V, and a duty cycle of 50%, while a constant voltage of 2.12 V was set in SF electrodeposition. The flow rate was 400 $L{\cdot}h^{-1}$ under the SF and TE&SF conditions. The actual waste liquid was treated using TE&SF electrodeposition. The process was conducted in sequence batch mode, and five batches of experiments were performed continuously. The Cu sheet was not replaced during this process. The transient electric field was in a square waveform at low and high voltages of 0 and 4 V, respectively, with a duty cycle of 50%. The flow rate was 400 $L{\cdot}h^{-1}$ and the total reaction time for one batch was 10–11 h.

2.3. Characterization of as-prepared products

The morphological evolution, chemical composition, elemental oxidative state, and phase analysis of the initial copper sheet and the as-prepared deposits under TE, SF, and TE&SF conditions were compared. The microstructure and surface chemistry were characterized by high-resolution field-emission scanning electron microscopy (FSEM; Zeiss Group, Germany) and energy-dispersive X-ray spectroscopy. Specific regions on the deposited surface were selected for elemental analysis and normalization to obtain the chemical compositions and contents of the deposited products. The surface roughness of the deposits was measured using surface three-dimensional topography (MicroXAM-3D; KLA, USA). X-ray photoelectron spectroscopy was employed for qualitative analysis of the surface elements of the as-formed deposits. Cu and O were evaluated using a monochromatic Al Kα X-ray source with a pass energy of 30.0 eV and step size of 0.05 eV. An X-ray diffractometer (XRD; Rigaku; SmartLab, Japan) equipped with Cu Kα ray with a wavelength of 0.15406 nm was used for phase analysis of the deposits, ranging from 3° to 90° at a scan speed of $0.02^{\circ}{\cdot}s^{-1}$.

2.4. Field analysis under transient electric field coupled with swirling mass transfer

COMSOL Multiphysics 6.0 software (COMSOL Inc., Sweden) was used to simulate the ion transport and interfacial reaction inside the reactor. Referring to the actual reactor, a three-dimensional model was established to describe the internal flow field and concentration changes in SF and non-SF. This process was simulated by the k–ε turbulence model, three-current distribution model based on electrical neutrality, and concentration cycle equation. For more accurate simulation of the reaction kinetics at the cathode boundary, the reactor model was simplified into a one-dimensional model in which the grids near the electrode were encrypted to capture the interfacial ion variations under SF and TE&SF conditions. In this model, the ion transport and electrodeposition kinetics were expressed by the Nernst–Planck and Butler–Volmer models, respectively, and an electric double-layer structure was established based on the electroneutral model of nitrate. Additionally, the chemical process in the electrolyte region followed the mass conservation, charge conservation, and electroneutral equations. Equations related to charge transfer and mass transfer are listed in Text S4 in Appendix A. The diffusion coefficient of the ions and the transfer coefficients of the cathodic and anodic reactions were set based on references and copper plating models, respectively [27,28]. The initial parameters of the model were set based on the experimental conditions (Table S1 in Appendix A).

3. Results and discussion

3.1. Sequential metal recovery from multi-component wastewater under transient electric field and swirling mass transfer

We measured the CV curves of copper deposition in different electrolyte systems to understand the relationship between the progress of electrode reaction and the potential (Fig. 2(a)). In the $Ni(NO_3)_2$ electrolyte, the curve maintained a low current level from –0.2 to 0.5 V vs reversible hydrogen electrode (RHE), which, subsequently, started to decrease at –0.2 V vs RHE, indicating that the charge transfer reaction occurred at –0.2 V vs RHE. A reduction peak was observed at –0.52 V vs RHE, indicating that the diffusion limit of Ni^{2+} was reached at this potential. In the solution containing only $Cu(NO_3)_2$, the current was significantly higher than that in the $Ni(NO_3)_2$ solution, implying that the charge transfer reaction was more efficient between Cu^{2+} and the electrode. When the potential negatively shifted across 0.4 V vs RHE, the reduction current continuously increased with the moving potential, with a turning point appearing at –0.43 V vs RHE because of ion diffusion. The CV curve in the solution containing $Cu(NO_3)_2$ and $Ni(NO_3)_2$ was closer to that in $Cu(NO_3)_2$ solution, indicating that the reduction of Cu^{2+} was dominant in the binary heavy metal solution. As the potential shifted positively, the crossover point in the CV curve revealed a surface change in the working electrode because Cu nuclei grew on the electrode surface [29].

Compared with that of the TE and SF electrodeposition processes, the kinetic performance of TE&SF electrodeposition improved significantly (Fig. 2(b), Fig. S1 in Appendix A). The recovery efficiency and kinetic coefficient of TE&SF electrodeposition were 97.04% and 0.0097 min^{-1}, respectively, which were approximately 5- and 13–20-fold higher than those of SF electrodeposition at a constant voltage of 2 V (Fig. S2 in Appendix A). The metal kinetic performance obtained at a constant 2.83 V enhanced conspicuously compared with that at 2 V, but its recovery efficiency and kinetic coefficient were still lower by 12%–20% and 37%–97%, respectively, in contrast with those of TE&SF electrodeposition. In contrast, the recovery efficiency of SF electrodeposition at 4 V was 87.8%, that is, 10.4% lower than that of TE&SF electrodeposition. However, blue and white precipitates were observed on the surface of the deposit (Fig. S3 in Appendix A), indicating that the electrochemical reaction had entered the side-reaction stage. Under these conditions, metal reduction and hydrogen evolution occurred simultaneously. Metal ions not only accepted electrons but also reacted with hydroxide ions to form metal hydroxides. Additionally, the metal deposition kinetics slowed in the TE electrochemical system, where the metal recovery efficiency and kinetic coefficient were only 51.2% and 0.0022 min^{-1}, respectively. In contrast to the recovery efficiency and kinetic coefficient of TE&SF electrodeposition, the values decreased by more than 83% and 250%, respectively. As shown in Figs. 2(c) and (d), the concurrent cathodic potential and current during TE, SF (2.83 V), and TE&SF electrodeposition partially reflected the kinetic trend. The cathodic potential at a constant 2.83 V was relatively positive compared with that under a transient electric field, resulting in relatively lower electron energy and subsequent slight interior charge transfer during electrodeposition [30]. Overall, the introduction of potential oscillations improved the dynamic behavior of metal deposition under the same mass-transfer conditions. Combined with the power consumption and metal deposition kinetics, we compared the specific energy consumptions under different operating conditions. Energy consumption includes electrochemical reactions, enhanced mass transfer, and the internal resistance of the electric device. For a metal solution with a concentration of 5.0 $g{\cdot}L^{-1}$, the specific consumption of TE, SF, and TE&SF electrodeposition was above

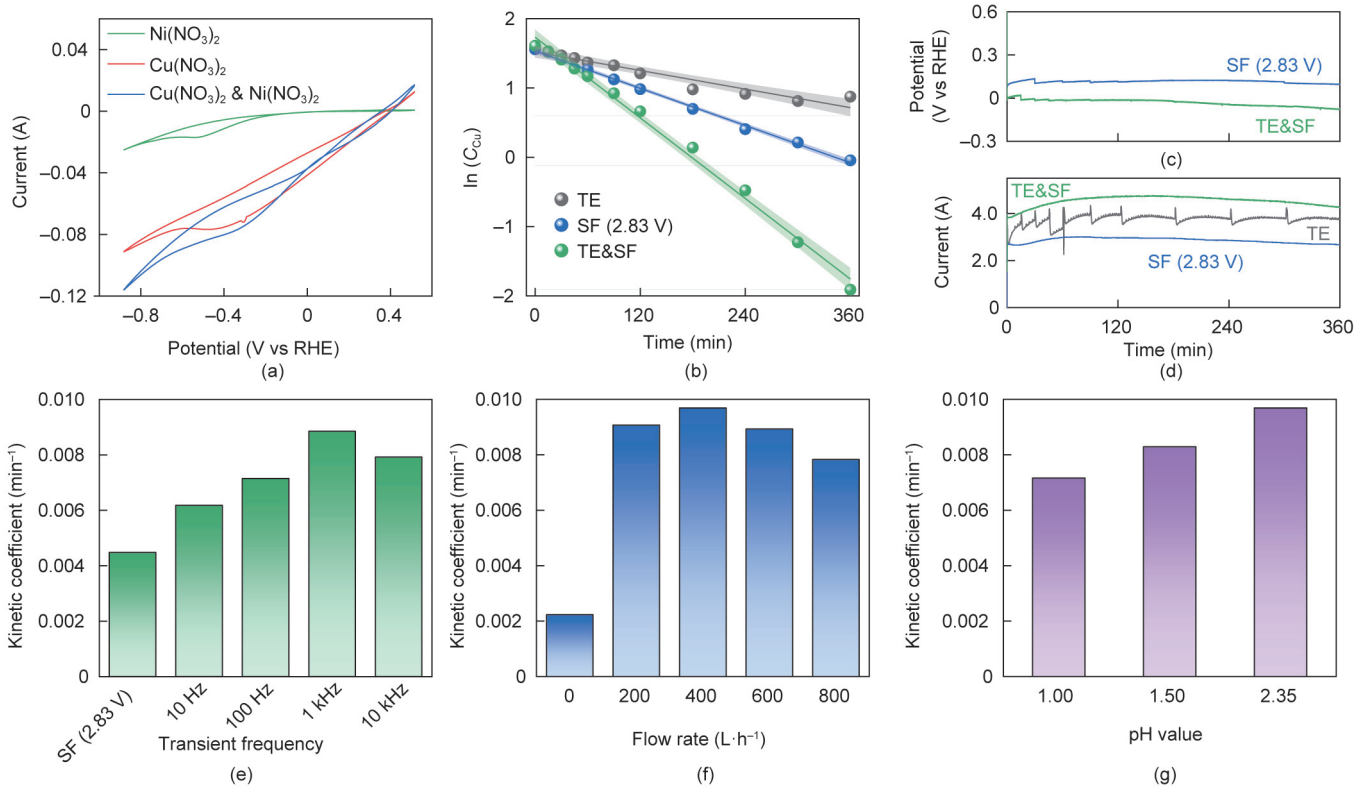

Fig. 2. Reaction kinetics of the electrodeposition system with transient electric field coupled with swirling mass transfer. (a) CV curves of the metal redox reaction in the Cu $(NO_3)_2$, $Ni(NO_3)_2$, and $Cu(NO_3)_2$ and $Ni(NO_3)_2$ solutions. (b) Cu^{2+} concentration (C_{Cu}) curves, (c) concurrent cathodic potential, and (d) current of metal electrodeposition under the conditions of TE, SF (2.83 V), and TE&SF. (e-g) Kinetic coefficients of metal electrodeposition with different (e) transient frequencies, (f) flow rates, and (g) pH values.

30 kW·h·kg^{-1} (Fig. S4 in Appendix A). Although electrodeposition under the SF condition has a relatively high electric power, its high recovery efficiency could compensate for this electric power, thereby achieving lower specific power consumption. Among the three operating modes, TE&SF electrodeposition exhibited the lowest specific power consumption.

To explore the effect of transient frequency on kinetic performance, we conducted copper TE&SF electrodeposition at different frequencies (Fig. 2(e), Fig. S5 in Appendix A). The kinetic coefficient exhibited a single peak at 10–10 000 Hz. When the transient frequency reached 100 Hz, the recovery efficiency and kinetic coefficient of Cu^{2+} deposition exceeded 90% and 0.0070 min^{-1}, attaining a maximum at 1 kHz. A comparison of the cathodic potential and current values (Fig. S6 in Appendix A) showed that the cathodic potential of electrodeposition under different frequencies was in the range ±0.15 V vs RHE. With an increase in frequency, the fluctuations in the potential and current decreased and reached a minimum at 1 kHz, indicating that the most stable TE&SF electrodeposition occurred at this frequency. The turning point of the reaction kinetics at 1 kHz has been reported in previous studies, and the existence of this turning point can be explained from two aspects. First, the timescale of the square-wave single period could affect the mechanism of metal deposition on the electrode surface. In the millisecond range, charge transfer and surface diffusion dominate during metal deposition. In the microsecond range, the rate-determining step of metal deposition is transformed into a first-step charge transfer reaction [31]. This conversion of the period scale results in a breakover point in kinetic performance. Second, the metal deposition induced by a transient electric field requires a critical time. When the effective electrodeposition time is less than the critical time, the ability of ions to cover the entire surface and reduce to elementary atoms is challenging [32]. In addition, an infinite increase in the transient frequency leads to a shorter time for Faradaic interfacial electron transfer because the initial current preferentially forms an electric double layer [33]. The time boundary required for metal crystal growth also leads to a frequency-turning point.

In contrast to the transient frequency, negligible differences were observed in the recovery efficiency and kinetic coefficient of Cu^{2+} at different flow rates (Fig. 2(f), Fig. S7 in Appendix A). In addition, the real-time cathodic potential and current did not change significantly along with increasing flow rates (Fig. S8 in Appendix A). Under enhanced mass transfer, the metal recovery efficiency could easily exceed 90%; however, further regulation of the hydraulic parameters did not improve the recovery efficiency or kinetics. The flow rate of the reactor was in the range 200–800 L·h^{-1}, corresponding to Reynolds numbers in the range 10^4–10^7. Therefore, the flow rate could not change the flow mode of the bulk solution, and the regulation space for the interfacial kinetic performance was limited. The recovery kinetics reached an extreme value at 400 L·h^{-1} because the flow rate was maximized for the fully loaded electrolyte. When the flow rate exceeded 400 L·h^{-1}, the electrolyte mixed with air in the circulating pump and reactor, resulting in inefficient operation and partial energy loss in the circulating pump. As shown in Fig. 2(g) and Fig. S9 in Appendix A, the metal recovery efficiency and kinetic coefficient gradually increased with an increase in pH from 1.00 to 2.35. In contrast, the cathodic potential and current increased significantly along with decreasing pH, reinforcing hydrogen evolution in the reaction system (Fig. S10 in Appendix A) and indicating that a change in pH could affect the reaction progress. The EDTA content affected the deposition morphology and kinetic performance through complexation with the metal ions. As the EDTA concentration increased, the kinetics of TE&SF electrodeposition slowed down (Fig. S11 in Appendix A).

In addition to rapid deposition kinetics, TE&SF electrodeposition helped to realize sequential metal recovery. Therefore, the residual Ni ions were recovered from the raffinate after the recovery of Cu. Considering the complex uncertainties of the Ni^{2+} deposition process, we adopted a constant-current electric field to stabilize the microscopic behavior of Ni^{2+} deposition (Fig. S12 in Appendix A). The reaction kinetics of Ni^{2+} reduction increased along with an increase in current density. As the current density increased to 75 mA·cm^{-2}, the kinetic coefficient and recovery efficiency of Ni deposition were 0.00621 min^{-1} and 89.3%, respectively. By controlling reasonable electric parameters, we regulated fast sequential metal recovery, thereby achieving efficient separation and resource utilization from complex industrial wastewater. In summary, TE&SF electrodeposition obtained accelerated Cu deposition kinetics and Cu–Ni separation at a transient potential of 0 and 4 V, as the low and high electric levels, a duty cycle of 50%, frequency of 1 kHz, and flow rate of 400 L·h^{-1}. The remaining Ni^{2+} was recovered by constant-current electrodeposition to achieve a recovery efficiency exceeding 85%.

3.2. Characterization and analysis of as-formed deposits

To comprehensively understand the quality of the as-formed deposits, we compared their morphological and chemical properties using a series of characterization techniques. From the perspective of morphological evolution (Fig. 3(a)), the deposits obtained by TE&SF electrodeposition had the most uniform and flattest microstructures. As the reactor was operated without swirling mass transfer, the grains of the electrodeposited copper were coarse and easily shaped into dendrites. As the reaction system lacked potential oscillation, the grain size of the deposit was relatively refined compared with that limited by mass transfer. Comparing the topography and roughness of these deposits (Fig. 3(b), Fig. S13 in Appendix A), TE electrodeposition recovered the metal with the roughest surface, whereas the roughness of the deposits was similar and relatively flat for SF and TE&SF. Although SF electrodeposition recovered metals with minimal roughness, the deposited Cu exhibited inferior morphological uniformity compared with that recovered under TE&SF electrodeposition. In general, the SF induced the formation of finer grains in the deposited metal, whereas the TE field achieved nanoscale morphological control to prevent the formation of nanoscale protrusions that roughen the deposit surface [34]. With further expansion of the observation field of the deposit morphology (Fig. S14 in Appendix A), some holes and microsized protrusions appeared on the deposit surface from SF electrodeposition, whereas the deposit from TE&SF electrodeposition was denser and flatter. Comparing the macroscopic appearance of the deposits under different working conditions, the deposit under the TE condition exhibited the lowest roughness and metal homogeneity. The uniformity of the SF electrodeposition deposit was significantly worse than that of the deposit obtained under the TE&SF condition. As regards the Ni deposit recovered from the raffinate, the nanoscale particles were larger than the Cu particles obtained under the TE&SF mode. However, the macroscopic appearance exhibited good uniformity and flatness (Fig. S15 in Appendix A). Comparing the chemical compositions (Fig. 3(c)), the deposits with the SF had a higher oxygen content because the circulating pump promoted the air mixture accompanied by kinetic energy supply to the electrolytes. Although a low oxygen content was obtained from the deposit under TE electrodeposition, poor Cu–Ni separation occurred because of the lack of SF confined to the replenishment of Cu^{2+} and the discharge of local alkaline ions [35]. The as-formed Ni deposit mainly comprised nickel, indicating that the sequential recovery of the

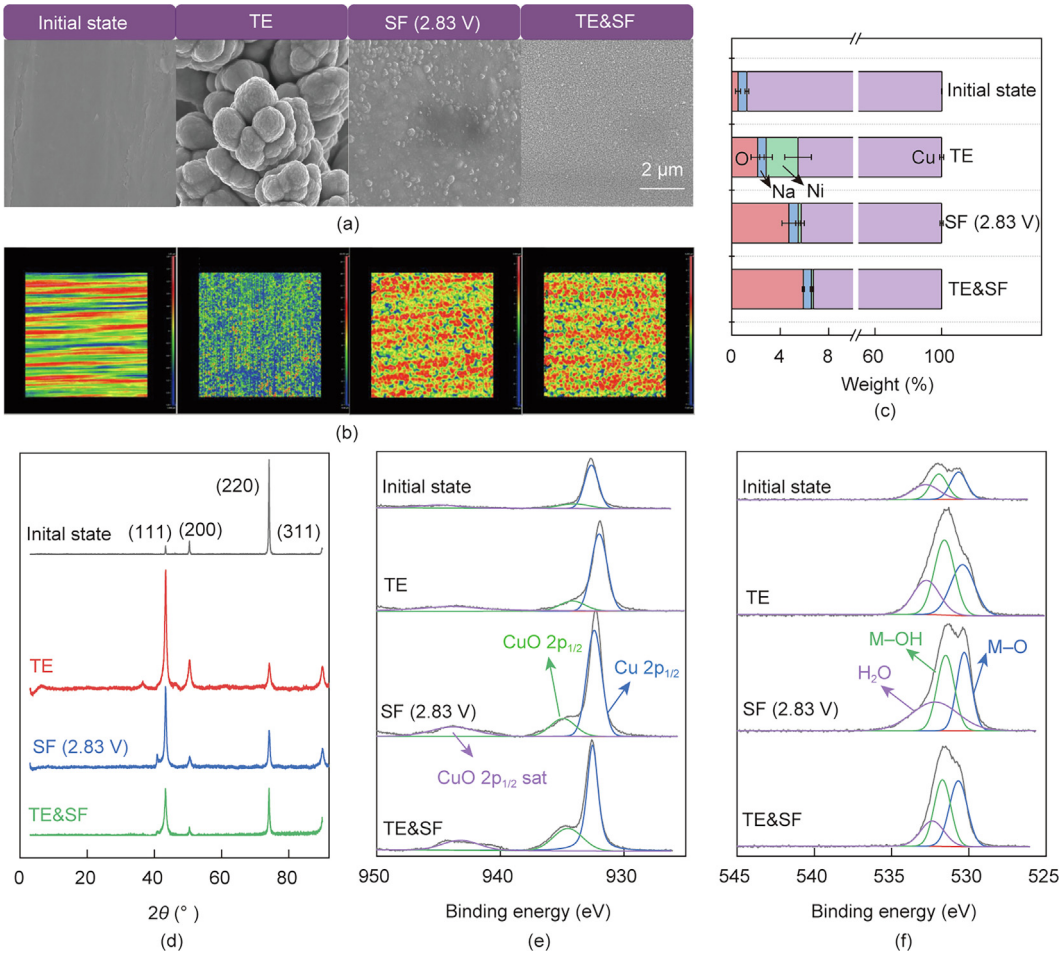

Fig. 3. Physical and chemical properties of as-formed deposits. (a) Micro morphology, (b) topography, (c) surface chemical composition, and (d) diffraction patterns of the deposits from TE, SF, and TE&SF electrodeposition. (e, f) The oxidative states of (e) Cu 2p and (f) O 1s in the as-formed deposits obtained from TE, SF (2.83 V), and TE&SF electrodeposition, where the black dashed line and red line represent primary data and fitting date, and M marked in the image represents the metal (Cu).

Ni-containing raffinate mainly yielded metallic nickel rather than nickel hydroxide (Fig. S16 in Appendix A).

As shown in Fig. 3(d), diffraction peaks assigned to the (111), (200), (220), and Cu(311) lattices were detected on the initial electrode and final deposited copper surface. The relative intensity ratios of the diffraction lattices reflected the morphological evolution of the Cu deposits. Initially, the electrode was placed in a quasi-single-crystal plane with the preferred Cu(220) orientation. As electrodeposition progressed, the Cu ions grew along the Cu(111) and Cu(220) facets because of the most conspicuous variation in their diffraction intensity. When the electrochemical system lacked the swirling mass transfer or transient electric field, the relative intensity ratio of Cu(111) and Cu(220) transformed to 4.55 and 2.00 from the initial ratio of 0.09. This phenomenon illustrated that the electrodeposited Cu atoms grew along the densely accumulated lattice, leading to the transformation of the preferred orientation. Consequently, TE and SF electrodeposition recovered a Cu deposit with relatively coarse grains and a rough surface. In contrast, the relative intensity ratio of the Cu(111) and Cu(220) facets in the deposit obtained under the synergistic effect of potential oscillation and SF was approximately 0.97, implying that the as-deposited Cu was more polycrystalline, with the Cu(111) and Cu(220) facets as the preferred orientation. The growth of polycrystalline Cu induces a uniform morphological evolution [36]. Cu(111) is the most energetically favorable plane for face centered cubic (FCC) metals; therefore, the growth of atoms deposited along Cu(111) is thermodynamically dominant [37,38]. Additionally, the reasons for growth along other lattices are unique and include fast quantum mechanical tunneling and lattice matching [38]. Moreover, an increase in the growth orientation of other crystal planes promotes the formation of uniform deposits. The enhanced surface energy and reduced concentration polarization supplied by the coupling of potential oscillation and swirling flow improve rapid electron transfer and refine the deposit surface.

Figs. 3(e) and (f) show the oxidative states of Cu 2p and O 1s, respectively, in the as-formed deposits. Characteristic peaks of Cu and Cu oxides were detected at 932.5 and 934.5 eV [39,40]. The Cu oxide content was higher in the deposits from SF and TE&SF electrodeposition, which coincided with the chemical composition results. Importantly, the electrodeposited Cu from TE&SF electrodeposition possessed a higher binding energy, indicating stronger interaction of the Cu atoms. In most cases, the O in the deposit originated mainly from M–O (530.6 eV) and M–OH (531.7 eV) [41]. In the absence of swirling flow, the M–OH content on the deposited Cu was higher than that of the others, which was ascribed to the accumulation of hydroxides in the cathode region under this condition.

3.3. Simulation of electrodeposition process under swirling flow and transient electric field

To gain more microscopic insight into Cu deposition under the synergy of interfacial potential oscillation and bulk mass transfer, we established a model that included turbulence. The model

included an electrochemical reaction module to simulate the distribution of the bulk flow field and interfacial concentration field under non-SF, SF, and TE&SF conditions (detailed equations are presented in Text S4). Electrode dynamics were applied to the Butler–Volmer equation, in which the exchange current density is determined by the mass action law. The electric double-layer region considers three mass-transfer forms of diffusion, migration, and convection and considers the laws of electrical neutrality and mass conservation. The bulk mass transfer applied k–ε turbulence model and introduced additional transport equations and two dependent variables of turbulent kinetic energy and the dissipation rate. In addition, a wall equation was established to connect the mass transfer between the bulk and interfacial phases. Under the SF condition, the intake conditions affected the turbulence model and interfacial mass transfer, and the flow field was exhibited in the form of a flow velocity distribution. As shown in Fig. 4(a), the flow rates at the inlet and outlet were higher than those in the other parts of the reactor because of the small diameters of the inlet and outlet. The kinetic energy of the fluid decreased from the bottom to the top of the reactor to overcome the one-way resistance and height difference. Moreover, the flow rate was distributed evenly inside the reactor from 0.15–0.30 $m \cdot s^{-1}$, which not only rapidly replenished the Cu^{2+} consumed in the deposition reaction but also refined the Cu grains and formed a uniform deposit. With SF, the Cu^{2+} concentration on the cathode surface tended to decrease from the bottom to the top, which conforms to the basic understanding of mass transfer and electrochemical reactions (Fig. 4(b)). Comparing the concentration-streamline distributions with and without SF, the degree of turbulent flow gradually decreased along the reactor because the streamline became sparser from the bottom to the top of the reactor. In addition, the Cu^{2+} concentration decreased with the streamline, indicating that Cu^{2+} ions were consumed continuously in the electrochemical reaction (Fig. 4(c)). In contrast to the continuous streamline under the SF, only partial ion transport along the radial direction occurred in the model under static hydraulic conditions, indicating that material transfer was limited without the SF (Fig. 4(d)).

To investigate the dependence of ion transport and reaction kinetics on the SF, we quantified the bulk and surface concentrations of Cu^{2+} under SF and non-SF conditions. The reactant concentration changed because of the electrochemical reaction and followed the concentration cycle equation. As shown in Figs. 4(e) and (f), although the decrease in the bulk Cu^{2+} concentration under non-SF condition was slightly higher than that under the SF condition, the amount of deposited Cu under the static condition was significantly lower than that under SF electrodeposition for the same time. This was ascribed to the electrolyte being circulated in the storage tank and deposition reactor with a volume of 2 L under SF electrodeposition, whereas the effective volume corresponding to the contact volume between the electrolyte and electrodes was only approximately 0.386 L under static conditions. However, the Cu^{2+} concentration on the cathode surface under static conditions decreased rapidly to 16 $mmol \cdot L^{-1}$ within 2 s and subsequently remained stable, whereas the concentration under SF conditions decreased more slowly. Electromigration and diffusion were the main mass-transfer processes at the interfaces, particularly in static deposition because enhanced convection was not prominent. In contrast, convection played the main role in mass transfer during SF deposition; therefore, the driving force of ion diffusion at the interface was smaller than that without SF, and concentration polarization was not significant during SF deposition [16].

The TE field changed the electrode dynamics through the pulse stimulus in the form of a current and subsequently acted on the reactant concentration. As shown in Fig. 4(g) under SF electrodeposition, migration, diffusion, and electrochemical reactions occurred continuously in the reactor; therefore, the Cu^{2+} concentration at the cathode interface and in the bulk phase decreased with time. During TE&SF electrodeposition, the Cu^{2+} concentration in the surface and bulk phases varied with the different stages of the

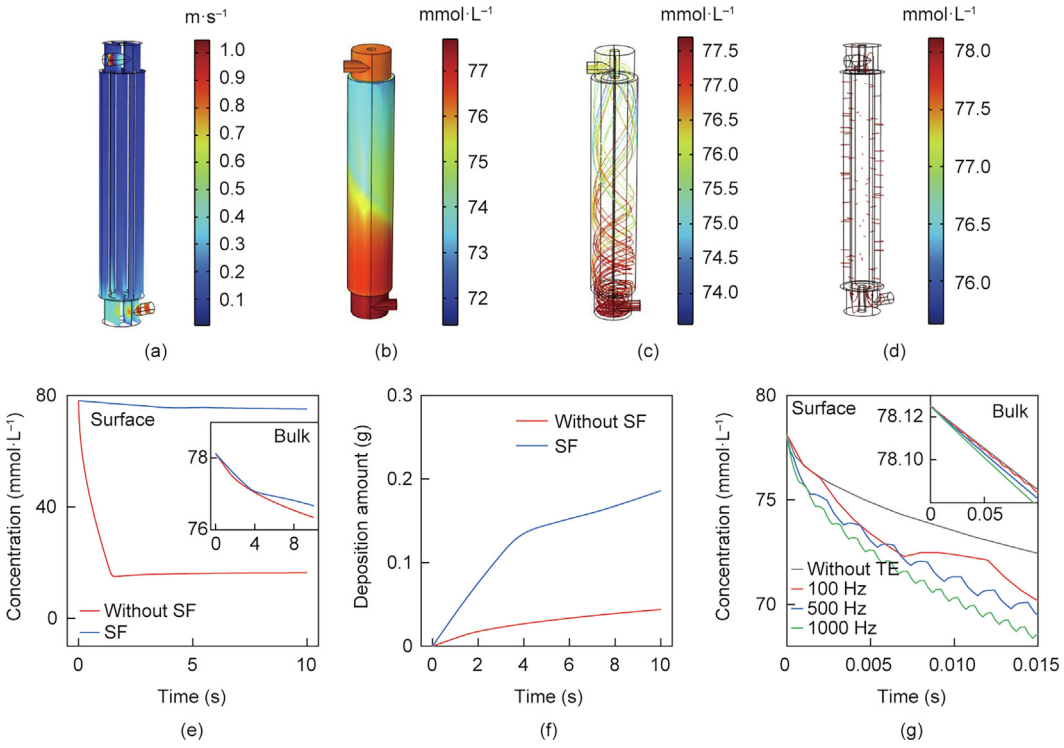

Fig. 4. Flow field and concentration field inside the reactor and on the cathodic surface. (a) Flow rate and (b) surface concentration distribution under SF. (c, d) Concentration-streamline distribution (c) with or (d) without SF. (e) Changes in the bulk and surface concentration and (f) deposition amounts with/without SF. (g) Changes in the bulk and surface concentration with/without TE.

periodic electric field. At a low potential in TE, the electrode surface underwent migration and diffusion, as well as rapid charge transfer and electrochemical reactions, resulting in the rapid consumption of Cu^{2+}. At high potentials, the electrochemical reactions ceased on the electrode surface. Diffusion supplemented the ion flux consumed in the previous stage; therefore, the Cu^{2+} concentration increased slowly at this stage. The deposition kinetics of TE&SF electrodeposition were higher than those of SF electrodeposition because rapid electrochemical reduction and high-concentration-driven ion transport occurred alternately on the electrode surface to ensure that the interface underwent cyclic metal deposition and reactant replenishment [26,42]. As the transient frequency increased to 1 kHz, the deposition kinetics increased gradually, which is consistent with the phenomenon mentioned above. Additionally, owing to the overpotential change and instantaneous potential change caused by TE, the symmetry factor of the interfacial electron transfer changed, which affected the electron transfer coefficient of the multistep electrode reaction and was possibly responsible for the improved kinetics during TE electrodeposition [28].

3.4. General applicability of electrodeposition under transient electric field and swirling mass transfer

To discuss the general applicability of TE&SF electrodeposition, the inherent properties of metal electrochemistry and solution properties should be considered to analyze the specific reactions on the electrode surface. In general, any metal ion could be reduced or deposited on the electrode if the electrode potential was sufficiently negative. However, when the reduction potential of the solvent is higher than that of the metal reduction, solvent decomposition occurs before metal reduction. In acidic aqueous solutions, metal ions with redox potentials higher than those of hydrogen evolution and water reduction are suitable for TE&SF electrodeposition. Apart from the separation and recovery of Cu/Ni binary solution, this TE&SF electrochemical strategy also has wide applicability in the recovery of precious metals, such as platinum ($E_{Pt^{2+}/Pt}$ = 0.58 or 0.73 V in Br- or Cl-containing solution), silver ($E_{Ag^{+}/Ag}$ = 0.80 V), and gold ($E_{Au^{3+}/Au}$ = 1.50 V). For metals with a redox potential lower than that of the solvent reduction, metal hydroxide precipitation is extremely easy because of the local alkalinity caused by hydrolysis during deposition. For metals such as lead ($E_{Pb^{2+}/Pb}$ = −0.13 V) and cobalt ($E_{Co^{2+}/Co}$ = −0.28 V), it is necessary to introduce additives to suppress hydrogen evolution and to set relatively high-energy electric parameters to ensure their rapid deposition. Owing to the change in solvation structure or solvation energy caused by the introduction of additives, the specific behavior of metal ions under the synergistic effect of TE&SF requires specific analysis and investigation. Additionally, for multi-metal wastewater, it is necessary to determine the sequence of metal deposition based on the redox potential and metal concentration. By controlling the cathodic potential in the range of the two adjacent redox potentials, the electric parameters were determined to achieve the graded recovery of multicomponent metals. Moreover, the metal deposition process should not enter the side-reaction stage, else hydroxide impurities are generated. In summary, for the recovery of a multi-metal solution, two boundary conditions, namely the metal redox potential and the deposition side reaction stage, should be considered fully.

Based on the above discussion, we conducted TE&SF electrodeposition of Ag-containing solutions to illustrate their applicability in recovering previously reported metals (Fig. S17 in Appendix A). Compared with the deposition performance under different operation modes, TE&SF electrodeposition possessed the most rapid recovery kinetics, with a kinetic coefficient and recovery efficiency of 0.099 min^{-1} and 95.40%, respectively. Its kinetic coefficient was 14.8 and 1.3 times those of the TE and SF processes, respectively, while the recovery efficiency was 4.70 and 1.06 times those of the TE and SF conditions, respectively. This outstanding experimental effect indicated that TE&SF electrodeposition could easily achieve high-value metal recovery from solutions containing precious metals, such as electroplating rinse water and gold leaching solution.

Additionally, to investigate the treatment effect of the TE&SF method on actual industrial wastewater, an electroplating rinse waste liquid with an initial Cu^{2+} concentration of approximately 30 $g{\cdot}L^{-1}$ from a three-waste purification enterprise in Kunshan City was treated using this combined method coupled with a TE field and turbulent flow. All treatments were performed in sequential batches, with each batch lasting 10–11 h. After electrodeposition, the final Cu recovery efficiency of each batch exceeded 99.0% (Fig. 5(a)), and the chromaticity of the wastewater had disappeared completely. The Cu metal recovered from TE&SF electrodeposition grew tightly on the surface of the copper sheet and was not dislodged with the swirling flow of wastewater (Fig. 5(b)).

Because the evaluation of energy consumption in most studies is limited to electrochemical reactions, we quantified the energy consumption of electrodeposition by integrating the product of the voltage and current per unit time to facilitate comparison (Text S3). The potential energy increased almost linearly with the progress of electrodeposition and the specific energy consumption ranged from 1.85−2.53 $kW{\cdot}h{\cdot}kg^{-1}$ (Fig. 5(c)). The energy consumption of TE electrodeposition was relatively low for wastewater treatment with similar heavy metal concentrations and pH ranges. Because the electrodeposition process in this study included bulk mass transfer and impedance of the power supply, we used a power meter for preliminarily evaluation of the energy consumption of the entire reaction process (Fig. 5(d)). The operation of the circulating pump consumed nearly 3.0 $kW{\cdot}h{\cdot}kg^{-1}$ of potential energy, and the overall energy consumption of TE&SF electrodeposition was approximately 9–10 $kW{\cdot}h{\cdot}kg^{-1}$. The overall energy consumption level of the TE&SF process was also low (5–10 $kW{\cdot}h{\cdot}kg^{-1}$) in the conventional electrochemical treatment of heavy metals [43].

In summary, the TE&SF deposition strategy proposed in this study achieved rapid and high-quality metal recovery without excessive energy consumption, thereby improving the comprehensive treatment capacity of wastewater containing heavy metals.

4. Conclusions

To overcome the limitations of interfacial ion transport on the reaction kinetics in the conventional electrodeposition process, we proposed a deposition strategy that couples the transient electric field with turbulent flow aimed at improving the bulk and interfacial ion transport and enhance the kinetics. By comparing the deposition kinetics and properties under a single transient electric field (TE), single swirling flow (SF), and their synergy (TE&SF), TE&SF electrodeposition not only achieved rapid metal recovery but also obtained high-quality deposits with homogeneous compositions and uniform morphologies. By simulating the flow and concentration fields inside the reactor and on the cathode surface, SF significantly reduced the concentration polarization of the reaction process and accelerated the reaction rate of metal deposition. In addition, potential oscillations at the interface realized alternating ion transport and efficient charge transfer. The synergistic effect of TE and SF effectively solved the limitation of ion transport at the interface on the reaction kinetics, thereby ensuring the efficient concurrence of ion transport and charge transfer. In addition, wide applicability was shown in

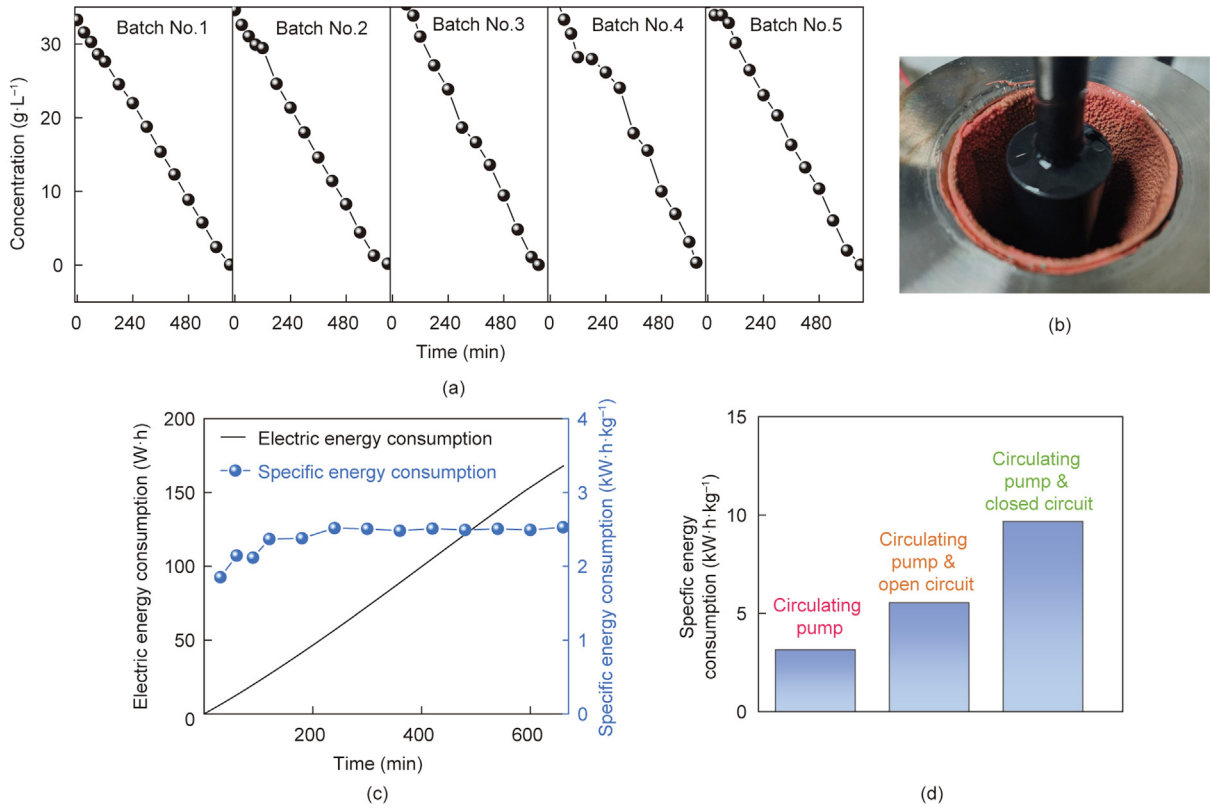

Fig. 5. Treatment of heavy metal wastewater under TE&SF electrodeposition. (a) Cu^{2+} concentration change under different electrodeposition batches, (b) image of Cu recovered from TE&SF electrodeposition, (c) electric energy and specific energy consumption during electrodeposition, and (d) energy consumption of the entire process.

recovering metals with redox potentials higher than those of hydrogen evolution and water reduction, achieving high-value recovery of precious and heavy metals.

Acknowledgments

This study was supported financially by the National Natural Science Foundation of China (52221004).

Compliance with ethics guidelines

Li Chen, Gong Zhang, Huijuan Liu, Shiyu Miao, Qingbai Chen, Huachun Lan, and Jiuhui Qu declare that they have no conflict of interest or financial conflicts to disclose.

Appendix A. Supplementary data

Supplementary data to this article can be found online at https://doi.org/10.1016/j.eng.2023.12.002.

References

[1] Ju J, Zhang Z, Pan Z, Che D, Li H. Determination of mineral resources in China's strategic emerging industries and analysis of the demand of the "14th Five Year Plan". China Ming Mag 2022;31(9):1–11.
[2] Guo X, Tian Q, Liu Y, Yan H, Li D, Wang Q, et al. Progress in research and application of non-ferrous metal resources recycling. Chin J Nonferrous Met 2019;29(9):1859–901.
[3] Xue B, Yang Q, Xia K, Li Z, Chen GY, Zhang D, et al. An AuNPs/mesoporous NiO/nickel foam nanocomposite as a miniaturized electrode for heavy metal detection in groundwater. Engineering 2023;27:199–208.
[4] Cai M, Li P, Tan W, Ren F. Key engineering technologies to achieve green, intelligent, and sustainable development of deep metal mines in China. Engineering 2021;7(11):1513–7.
[5] Vardhan KH, Kumar PS, Panda RC. A review on heavy metal pollution, toxicity and remedial measures: current trends and future perspectives. J Mol Liq 2019;290:111197.
[6] Zaynab M, Al-Yahyai R, Ameen A, Sharif Y, Ali L, Fatima M, et al. Health and environmental effects of heavy metals. J King Saud Univ Sci 2022;34(1):101653.
[7] Mitra S, Chakraborty AJ, Tareq AM, Emran TB, Nainu F, Khusro A, et al. Impact of heavy metals on the environment and human health: novel therapeutic insights to counter the toxicity. J King Saud Univ Sci 2022;34(3):101865.
[8] Zheng X, Zhu Z, Lin X, Zhang Y, He Y, Cao H, et al. A mini-review on metal recycling from spent lithium ion batteries. Engineering 2018;4(3):361–70.
[9] Sahajwalla V. Green processes: transforming waste into valuable resources. Engineering 2018;4(3):309–10.
[10] Yang L, Hu W, Chang Z, Liu T, Fang D, Shao P, et al. Electrochemical recovery and high value-added reutilization of heavy metal ions from wastewater: recent advances and future trends. Environ Int 2021;152:106512.
[11] Maarof HI, Daud WMAW, Aroua MK. Recent trends in removal and recovery of heavy metals from wastewater by electrochemical technologies. Rev Chem Eng 2017;33(4):359–86.
[12] Azimi A, Azari A, Rezakazemi M, Ansarpour M. Removal of heavy metals from industrial wastewaters: a review. Chembioeng Rev 2017;4(1):37–59.
[13] Saleh TA, Mustaqeem M, Khaled M. Water treatment technologies in removing heavy metal ions from wastewater: a review. Environ Nanotechnol Monit Manage 2022;17:100617.
[14] Bagali SS, Gowrishankar BS, Roy AS. Optimization, kinetics, and equilibrium studies on the removal of lead(II) from an aqueous solution using banana pseudostem as an adsorbent. Engineering 2017;3(3):409–15.
[15] Seeber R, Zanardi C, Inzelt G. The inherent coupling of charge transfer and mass transport processes: the curious electrochemical reversibility. ChemTexts 2016;2(2):8.
[16] Volgin VM, Davydov AD. Mass-transfer problems in the electrochemical systems. Russ J Electrochem 2012;48(6):565–9.
[17] Marcus RA. On the theory of oxidation-reduction reactions involving electron transfer. I. J Chem Phys 2004;24(5):966–78.
[18] Yu D, Lui Q, Su W, Wang L, Sun Y, Zhang Z. A review on research and application of electrodeposition for heavy metal wastewater treatment. Chem Ind Eng Progr 2020;39(5):1938–49.
[19] Ji Q, Yu D, Zhang G, Lan H, Liu H, Qu J. Microfluidic flow through polyaniline supported by lamellar-structured graphene for mass-transfer-enhanced electrocatalytic reduction of hexavalent chromium. Environ Sci Technol 2015;49(22):13534–41.
[20] Zhao X, Guo L, Qu J. Photoelectrocatalytic oxidation of Cu–EDTA complex and electrodeposition recovery of Cu in a continuous tubular photoelectrochemical reactor. Chem Eng J 2014;239:53–9.

[21] Zhang C, Jiang Y, Li Y, Hu Z, Zhou L, Zhou M. Three-dimensional electrochemical process for wastewater treatment: a general review. Chem Eng J 2013;228:455–67.
[22] Jin W, Su J, Chen S, Li P, Moats MS, Maduraiveeran G, et al. Efficient electrochemical recovery of fine tellurium powder from hydrochloric acid media via mass transfer enhancement. Separ Purif Tech 2018;203:117–23.
[23] Yáñez-Varela JA, Alonzo-Garcia A, González-Neria I, Mendoza-Escamilla V, Rivadeneyra-Romero G, Martínez-Delgadillo SA. Experimental and numerical evaluation of the performance of the electrochemical reactor operated with static and dynamic electrodes in the reduction of hexavalent chromium. Chem Eng J 2020;390:124575.
[24] Bard AJ, Faulkner LR. Electrochemical methods: fundamentals and applications. 2nd ed. New York City: John Wiley and Sons; 2001.
[25] Ning D, Yang C, Wu H. Ultrafast Cu^{2+} recovery from waste water by jet electrodeposition. Separ Purif Tech 2019;220:217–21.
[26] Behboudi-Khiavi S, Javanbakht M, Mozaffari SA, Ghaemi M. Controllable pulse reverse electrodeposition of mesoporous Li_xMnO_2 nano/microstructures with enhanced electrochemical performance for Li-ion storage. ACS Appl Mater Interfaces 2019;11(24):21552–66.
[27] Kalliomäki T, Wilson BP, Aromaa J, Lundström M. Diffusion coefficient of cupric ion in a copper electrorefining electrolyte containing nickel and arsenic. Miner Eng 2019;134:381–9.
[28] Bockris JO, Nagy Z. Symmetry factor and transfer coefficient. A source of confusion in electrode kinetics. J Chem Educ 1973;50(12):839.
[29] Chandran C, Singh HD, Leo LS, Shekhar P, Rase D, Chakraborty D, et al. A covalent organic framework with electrodeposited copper nanoparticles—a desirable catalyst for the Ullmann coupling reaction. J Mater Chem A Mater Energy Sustain 2022;10(29):15647–56.
[30] Gerischer H. Physical chemistry: an advanced treatise. New York City: Academic Press; 1971. p. 487–9.
[31] Tsai W, Wan C, Wang Y. Mechanism of copper electrodeposition by pulse current and its relation to current efficiency. J Appl Electrochem 2002;32(12):1371–8.
[32] Li L, Li G, Zhang Y, Yang Y, Zhang L. Pulsed electrodeposition of large-area, ordered $Bi_{1-x}Sb_x$ nanowire arrays from aqueous solutions. J Phys Chem B 2004;108(50):19380–3.
[33] Aryanfar A, Brooks D, Merinov BV, Goddard III WA, Colussi AJ, Hoffmann MR. Dynamics of lithium dendrite growth and inhibition: pulse charging experiments and monte carlo calculations. J Phys Chem Lett 2014;5(10):1721–6.
[34] Zou J, Zhang H, Wu Z, Wang J, Li B, Cui J, et al. Effects of an intermittent permanent magnet stirring on the melt flow and grain refinement of Al–4.5Cu alloy. J Mater Res Technol 2021;14:1585–600.
[35] Jin W, Hu M, Hu J. Selective and efficient electrochemical recovery of dilute copper and tellurium from acidic chloride solutions. ACS Sustain Chem Eng 2018;6(10):13378–84.
[36] Cai Z, Wang J, Lu Z, Zhan R, Ou Y, Wang L, et al. Ultrafast metal electrodeposition revealed by *in situ* optical imaging and theoretical modeling towards fast-charging Zn battery chemistry. Angew Chem Int Ed 2022;61(14):e202116560.
[37] Yan Y, Shu C, Zeng T, Wen X, Liu S, Deng D, et al. Surface-preferred crystal plane growth enabled by underpotential deposited monolayer toward dendrite-free zinc anode. ACS Nano 2022;16(6):9150–62.
[38] Tan M, Chen X. Growth mechanism of single crystal nanowires of fcc metals (Ag, Cu, Ni) and hcp metal (Co) electrodeposited. J Electrochem Soc 2011;159(1):K15–20.
[39] Penkala B, Gatla S, Aubert D, Ceretti M, Tardivat C, Paulus W, et al. *In situ* generated catalyst: copper(II) oxide and copper(I) supported on $Ca_2Fe_2O_5$ for CO oxidation. Catal Sci Technol 2018;8(20):5236–43.
[40] Zhu X, Gao X, Qin R, Zeng Y, Qu R, Zheng C, et al. Plasma-catalytic removal of formaldehyde over Cu–Ce catalysts in a dielectric barrier discharge reactor. Appl Catal B 2015;170–171:293–300.
[41] Bo X, Hocking RK, Zhou S, Li Y, Chen X, Zhuang J, et al. Capturing the active sites of multimetallic (oxy)hydroxides for the oxygen evolution reaction. Energy Environ Sci 2020;13(11):4225–437.
[42] Kawai S, Ogawa M, Ishibashi K, Kondo Y, Matsuoka T, Homma T, et al. Transient mass transfer rate of Cu^{2+} ion caused by copper electrodeposition with alternating electrolytic current. Electrochim Acta 2010;55(12):3987–94.
[43] Tonini GA, Ruotolo LAM. Heavy metal removal from simulated wastewater using electrochemical technology: optimization of copper electrodeposition in a membraneless fluidized bed electrode. Clean Technol Environ Policy 2017;19(2):403–15.